



Hot deformation behavior of TC11/Ti–22Al–25Nb dual-alloy in isothermal compression

Chun QIN, Ze-kun YAO, Yong-quan NING, Zhi-feng SHI, Hong-zhen GUO

School of Materials Science and Engineering, Northwestern Polytechnical University, Xi'an 710072, China

Received 22 September 2014; accepted 17 November 2014

Abstract: The high-temperature flow behavior of TC11/Ti–22Al–25Nb electron beam (EB) weldments was investigated by the isothermal compression tests at the temperature of 900–1060 °C and the strain rate of 0.001–10 s⁻¹. Based on the experimental data, the constitutive equation that describes the flow stress as a function of strain rate and deformation temperature is obtained. The apparent activation energy of deformation is calculated, which decreases with increasing the strain and the value is 334 kJ/mol at strain of 0.90. The efficiency of power dissipation η changes obviously with the variation of deformation conditions. Under the strain rates of 0.01, 0.1 and 1 s⁻¹, the value of η increases with increasing the true strain for different deformation temperatures. While the value of η decreases with increasing the strain under the strain rates of 0.001 and 10 s⁻¹. The optimum processing condition is ($t_{opi}=1060$ °C, $\dot{\epsilon}_{opi}=0.1$ s⁻¹) with the peak efficiency of 0.51. Under this deformation, dynamic recrystallization (DRX) is observed obviously in the microstructure of welding zone. Under the condition of 1060 °C and 0.001 s⁻¹, the deformation mechanism is dominated by dynamic recovery (DRV) and the value of η decreases sharply ($\eta=0.02$). The flow instability is predicted to occur since the instability parameter $\zeta(\dot{\epsilon})$ becomes negative. The hot working process can be carried out safely in the domain with the strain rate of 0.001–0.6 s⁻¹ and the temperature of 900–1060 °C.

Key words: dual-alloy; hot deformation; processing map; apparent activation energy; microstructure

1 Introduction

Electron beam welding (EBW) is a fusion joining process in vacuum environment with high density of energy, which can be used in nuclear and aerospace industries for complex structures with joining or surface melting [1,2]. If the EBW was used to joint different alloys, the combination might meet different kinds of property needs, making use of each material efficiently. A great number of researches have been conducted to the EBW techniques for metallic materials [3–5]. ZHAO and LIU [3] analyzed the fatigue properties, tensile properties and microstructure evolution of 06Cr19Ni10 austenitic stainless steel. WANG and WU [4] investigated the microstructure and mechanical properties of electron beam welded joints for Ti–6Al–4V alloy. ZHANG et al [5] explored the microstructure and tensile property of dissimilar joint weld between Ti₃Al and TC4. Generally, the EBW method can produce quality welds for titanium alloys without limit interstitial element

(mainly oxygen) ingress in vacuum environment, but the solidification micropores still existed in the fusion zone as the fast solidification rates. SABOL et al [6] studied the metallurgical aspects and localized tensile strain distribution of electron beam welded Ti–5Al–5V–Mo–3Cr titanium alloys. Meanwhile, fracture occurred in the weld area and was primarily due to the microvoid coalescence. The solidification of EBW is a nonequilibrium process. Columnar grains and metastable phases were formed which were detrimental to the mechanical properties. To eliminate those defects, the following hot working process including hot plastic deformation becomes a key process. LIU et al [7] and TAN et al [8] discovered that isothermal deformation and heat treatment had important influence on the microstructures and properties of dissimilar joints of TC11/Ti–24Al–15Nb–1.5Mo and TC11/Ti–22Al–25Nb alloys welded by the EBW process.

The high temperature deformation behaviors of metals and alloys are very complex during the hot forming process [9]. The processing map is a representation of

the response of material in respect of the microstructural evolution under the applied process parameters, which is based on the dynamic materials model (DMM) [10]. Processing map is a useful method to identify the deformation temperature–strain rate windows for hot working, which has been developed to optimize the hot working process of the metals or alloys in recent years. NING et al [11] analyzed the hot deformation behavior and working characteristic of nickel-based electron beam weldments using the processing map. In the present study, the EBW of the mechanically polished TC11 alloy and Ti–22Al–25Nb alloy was conducted. The hot deformation behavior of TC11/Ti–22Al–25Nb EB weldments was investigated based on the isothermal compression tests conducted at different deformation temperatures and strain rates. Based on the compression results and the related analyses, the flow behavior was investigated and the constitutive model was established. Moreover, the approach of processing map was adopted to explore the deformation mechanism during the hot compression processing and to optimize the hot process parameters for the EB weldments.

2 Experimental

The nominal compositions of TC11 alloy are (mass fraction) 6.5% Al, 3.5% Mo, 1.5% Zr, 0.3% Si and Ti balance; and the nominal compositions of Ti–22Al–25Nb alloy are (mole fraction) 22% Al, 25% Nb and Ti

balance. Figure 1 shows the typical microstructures of the two alloys. The TC11 alloy presents the typical bimodal microstructure consisting of equiaxed α and transformed β phase (Fig. 1(a)). The microstructure of Ti–22Al–25Nb alloy is composed of large grains with α_2 phase distributed at the grain boundary (Fig. 1(b)).

The block specimens with dimensions of 20 mm \times 60 mm \times 6 mm were prepared by mechanical polishing for EBW. The EBW process was conducted using a KS55–G150 model EBW machine with an accelerating voltage of 150 kV. The welding current was 28 mA, the focusing current was 2250 mA and the welding speed was selected as 8 mm/s. The cylindrical compression specimens with dimensions of ϕ 8 mm \times 12 mm were machined from the centre of the EB weldments. The fusion zone is in the middle of the cylindrical compression specimens (Fig. 1(d)). Figure 1(c) presents the microstructure of the fusion zone.

The isothermal hot compression tests were conducted on a Gleeble–3500 thermo-simulation machine at deformation temperatures of 900, 940, 980, 1020 and 1060 °C under strain rates of 0.001, 0.01, 0.1 and 1.0 s⁻¹. The height reduction for all the specimens was 60%. All the specimens were heated at a heating rate of 10 °C/s and soaked at the deformation temperature for 6 min in order to obtain a uniform temperature distribution in the entire specimen. The strain–stress curves were automatically recorded in the compression process for each deformation temperature and strain rate.

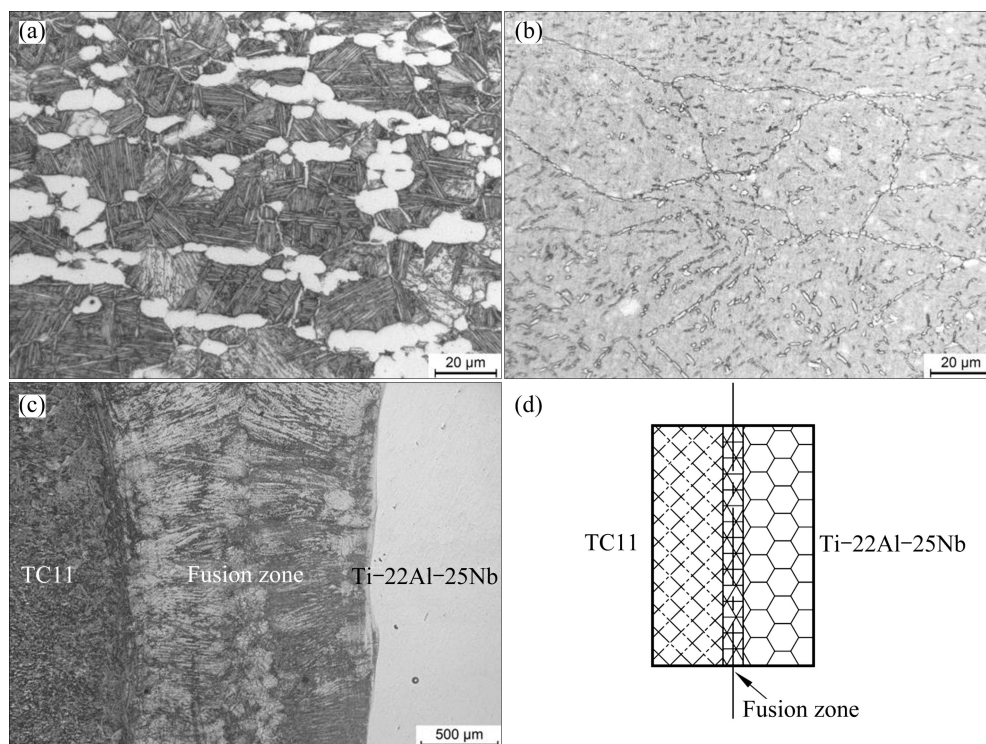


Fig. 1 Typical microstructures of as-received TC11 alloy and Ti–22Al–25Nb alloy and their electron beam weldments: (a) As-received TC11 alloy; (b) As-received Ti–22Al–25Nb alloy; (c) Electron beam weldments; (d) Schematic illustration of weldments for isothermal hot compression test

In the whole process of heating, the heat preservation and hot deformation were protected by the argon. The specimens were cooled down to room temperature by water spraying. The samples were sectioned parallel to the compression axis. The microstructure observations were conducted using an Olympus-PM3 optical microscope (OM).

3 Results and discussion

3.1 Flow behavior of TC11/Ti-22Al-25Nb dual-alloy

The typical true stress–true strain curves of

TC11/Ti-22Al-25Nb dual-alloy obtained at various deformation temperatures and strain rates are presented in Fig. 2. As shown in Fig. 2, the stress–strain curves are similar with each other and sensitive to the deformation temperature and strain rate. The flow stress exhibits an initial sharp increase with increasing the strain until a peak flow stress occurs at a very small strain. And the peak flow stresses decrease with an increase of deformation temperature, whereas they all increase with increasing the strain rate. In the following deformation, the stress decrease with increasing the strain until a relatively stable stress appears, showing a dynamic flow

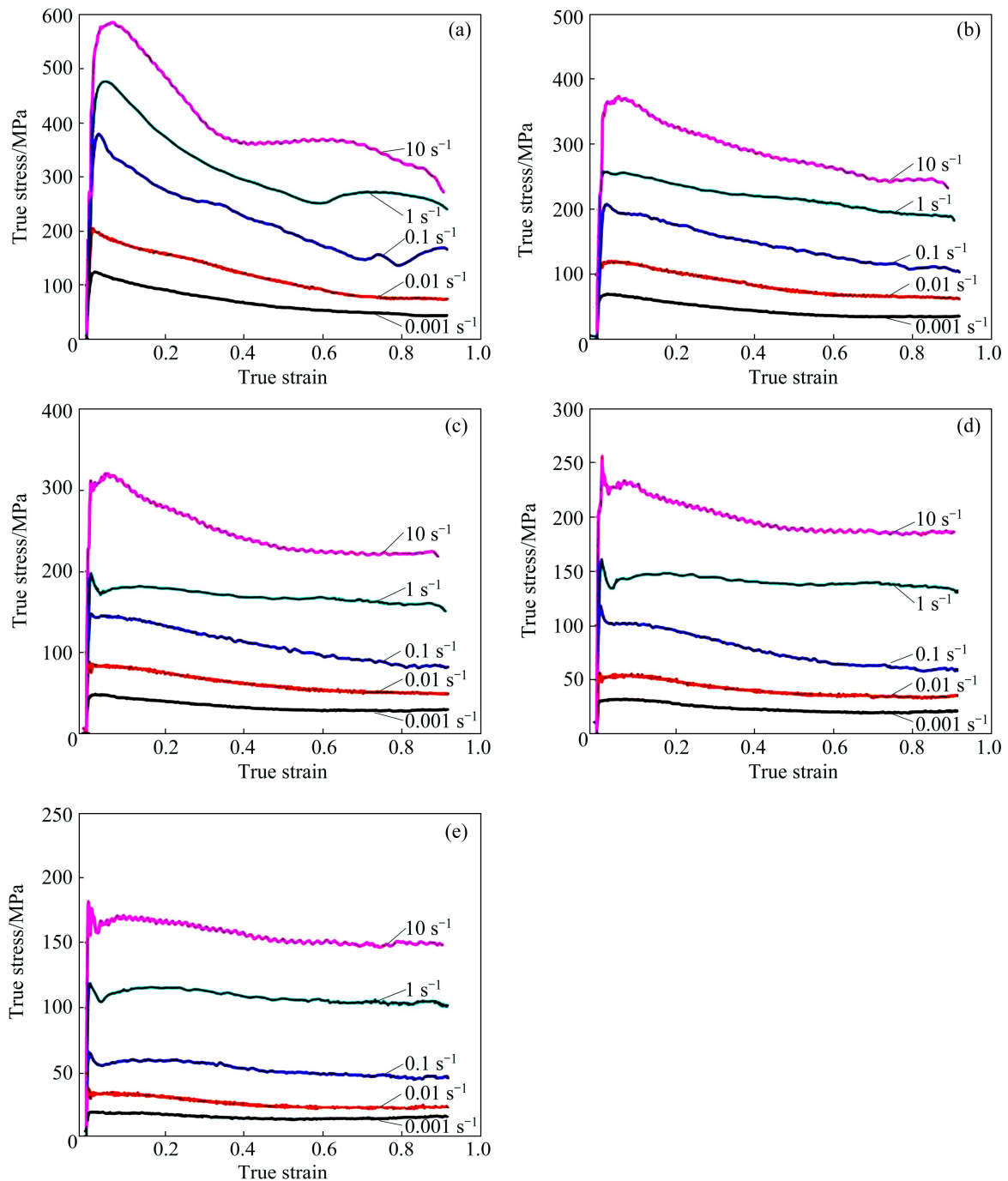


Fig. 2 True stress–true strain curves of TC11/Ti-22Al-25Nb dual-alloy electron beam weldments in isothermal hot compression at different temperatures: (a) 900 °C; (b) 940 °C; (c) 980 °C; (d) 1020 °C; (e) 1060 °C

softening. The true stress–true strain curves can indicate the intrinsic relationship between the flow stress and the thermal-dynamic behavior. At the beginning of hot compression, work hardening results in the rapid increase of flow stress. With increasing the true strain, the effect of flow softening causes that the flow stress decreases and tends to steady state. However, it is difficult to predict the deformation mechanism only by relying on the shape of stress–strain curves. For instance, the flow softening probably indicates dynamic recrystallization (DRX), lamellar globularization or adiabatic heating, etc [12,13]. Likewise, the steady state flow behavior may demonstrate superplasticity or dynamic recovery (DRV) [14]. Therefore, the flow stress behavior will be analyzed in detail in the following sections using the processing map combined with the microstructure analyses.

The deformation temperature obviously affects the steady flow behavior of EB weldments. The steady flow behavior is inconspicuous at low deformation temperatures (900 and 940 °C). As the deformation temperature increases, the steady flow stress occurs more quickly. Meanwhile, with a low strain rate ($\dot{\epsilon}=0.001\text{ s}^{-1}$), a steady stress state is achieved in which the flow stress remains nearly constant with increasing the strain at higher deformation temperature. These flow stress–strain curves indicate that the dynamic flow softening is sufficient to balance the work hardening effect. These results have a good agreement with the researches of TC11 alloy [15] and Ti–22Al–25Nb alloy [16]. Moreover, the EB weldments display oscillation flow stress at higher strain rate (10 s^{-1}) and over all deformation temperatures. The oscillations in the stress–strain curves are indications of dynamic recrystallization (DRX), unstable deformation, or cracking [17]. This phenomenon is consistent with the research results reported by LI et al [18] and JIA et al [19].

3.2 Constitutive equation of TC11/Ti–22Al–25Nb electron beam weldment

Arrhenius equation is widely used to describe the relationship among flow stress, strain rate and temperature at high temperature [20,21]. The effects of temperature and strain rate on deformation behavior can be represented by parameter Z (Zener–Hollomon). The hyperbolic law in the Arrhenius type equation gives a better approximation between parameter Z and flow stress.

$$\dot{\epsilon} = A[\sinh(\alpha\sigma)]^n \exp[-Q/(RT)] \quad (1)$$

$$Z = \dot{\epsilon} \exp[Q/(RT)] \quad (2)$$

where $\dot{\epsilon}$ is the strain rate (s^{-1}), Q is the deformation activation energy (kJ/mol), R is the mole gas constant (kJ/(mol·K)), T is the thermodynamic temperature (K),

and σ is the stress for a given strain, A , α and n are the material constants which are independent of the deformation temperature.

The constants of the hyperbolic sine equation can be determined by the regression analysis of data using natural logarithm. It can be seen that when the deformation temperature T is constant, there exists a linear relation between the natural logarithm of strain rate ($\ln\dot{\epsilon}$) and the natural logarithm of flow stress ($\ln\sinh(\alpha\sigma)$), and the following relation can be obtained:

$$n = \left[\frac{\partial \ln \dot{\epsilon}}{\partial \ln[\sinh(\alpha\sigma)]} \right]_T \quad (3)$$

When the strain rate is constant, the hot deformation activation energy can be expressed by taking partial derivative of Eq. (1):

$$Q = Rn \left[\frac{\partial \ln[\sinh(\alpha\sigma)]}{\partial (1/T)} \right]_{\dot{\epsilon}} \quad (4)$$

The following is taking the strain of 0.9 as an example to introduce how to determine the material constants. The amount of α is determined to be 0.011 from plots of $\ln\sigma$ versus $\ln\dot{\epsilon}$ and σ versus $\ln\dot{\epsilon}$ at different deformation temperatures. By linear regression of data from $\ln[\sinh(\alpha\sigma)]$ versus $\ln\dot{\epsilon}$, the average of slopes gives the n value of 3.05. In a similar way, by plotting $\ln[\sinh(\alpha\sigma)]$ versus $1/T$ (Fig. 3), the slope gives the value of $Q/(nR)$, where the apparent activation energy of process is determined to be 334 kJ/mol. In the previous researches, the apparent activation energies of Ti₂AlNb-based alloys have been examined to be 250–540 kJ/mol [19,22,23], while the apparent activation energies of TC11 alloy have been examined to be 471.6 kJ/mol [24] in the $\alpha+\beta$ phase region and 172.3 kJ/mol [25] in the β phase region. The value of apparent activation energy for TC11/Ti–22Al–25Nb EB weldments in this work is between the values reported in the previous researches. Figure 4 shows the relationship

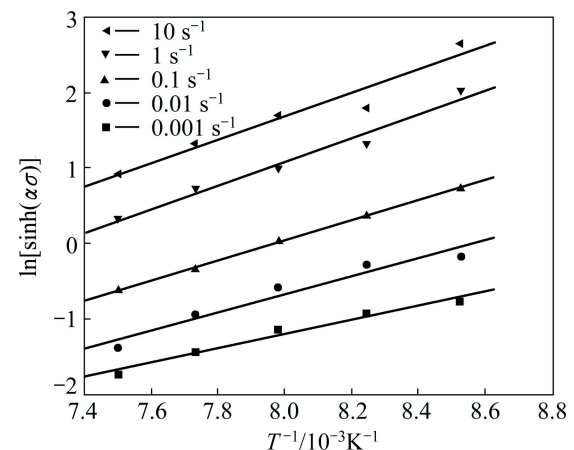


Fig. 3 Relationship between $\ln[\sinh(\alpha\sigma)]$ and $1/T$

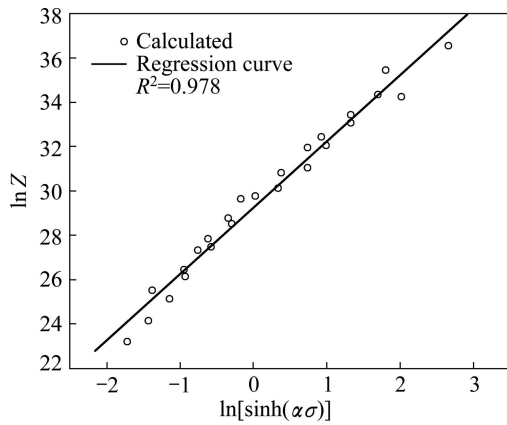


Fig. 4 Plot of Zener–Hollomon parameter as function of flow stress

between the strain rate temperature parameter Z and the flow stress with a correlation coefficient of 0.978. From the linear regression of data, the material constant A can be obtained as 5.20×10^{12} . Based on the experimental results, a constitutive equation that describes the flow stress as a function of strain rate and deformation temperature in the isothermal hot working process can be expressed as

$$\dot{\varepsilon} = 5.20 \times 10^{12} [\sinh(0.011\sigma)]^{3.05} \exp\left(\frac{-3.34 \times 10^5}{RT}\right) \quad (5)$$

If the above mentioned process of calculation is repeated for different strains, the apparent activation energy Q can be obtained associated with the strain. The apparent activation energies for TC11/Ti–22Al–25Nb EB weldments are calculated with different strains of 0.1–0.9. The apparent activation energy with standard deviation for deformation at different strains is illustrated in Fig. 5. Also, the relationship between the apparent activation energies and the true strains for the EB weldments can be expressed as the 5th order polynomial function fitted as shown in Eq. (6). It is easy to find out that the regression curve fits the experimental data very well. From Fig. 5, it can be seen that the apparent activation energy for deformation decreases from (627 ± 140) kJ/mol to (334 ± 66) kJ/mol as the strain increases from 0.1 to 0.9. The similar variation of apparent activation energy for Ni–Cr–Co-based P/M superalloy has been obtained [26]. The main reason is considered that only a small number of soft-oriented slip systems and grains take part in the deformation in the initial stage of deformation, so the value of apparent activation energy is high. And then grain rotation occurs and more slip systems are activated with increasing the deformation strain, resulting in the decrease of apparent activation energy.

$$Q = 744.8 - 1487.6\varepsilon + 3936.7\varepsilon^2 - 7137.5\varepsilon^3 + 6703.4\varepsilon^4 - 2466.9\varepsilon^5 \quad (6)$$

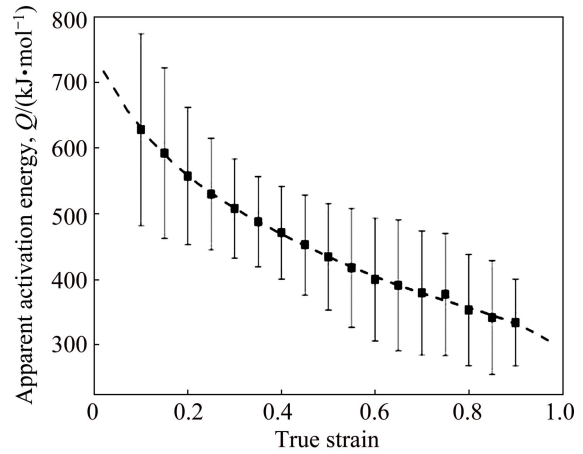


Fig. 5 Relationships between apparent activation energy (Q) and true strain of electron beam weldments

By applying the determined material constants of the constitutive equations, the flow stress can be calculated for different deformation temperatures at the strain rate of $0.001\text{--}10 \text{ s}^{-1}$. Figure 6 shows the comparison of the experimental stress–strain data with the calculated results for four different strain rates at $940 \text{ }^\circ\text{C}$. In order to evaluate the accuracy of the deformation constitutive equation, the error between the calculated flow stress (σ_c) and the measured flow stress (σ_m) can be calculated. Table 1 lists the results of this evaluation for flow stress calculated at strains of 0.1, 0.3, 0.5, 0.7 and 0.9 with strain rates of 0.001, 0.01, 0.1, 1 and 10 s^{-1} at $940 \text{ }^\circ\text{C}$. It can be easily found that, for the worst case, the error in the flow stress estimate is 10.76% at the strain of 0.1. As the flow stress decreases and tends to be steady state, the error has a decreasing tendency. At the strain of 0.7, the error is 4.81%. It can be found that the predicted results have a good agreement with the experimental data. The results indicate that the proposed deformation constitutive equation gives an accurate estimate of the flow stress for TC11/Ti–22Al–25Nb EB weldments.

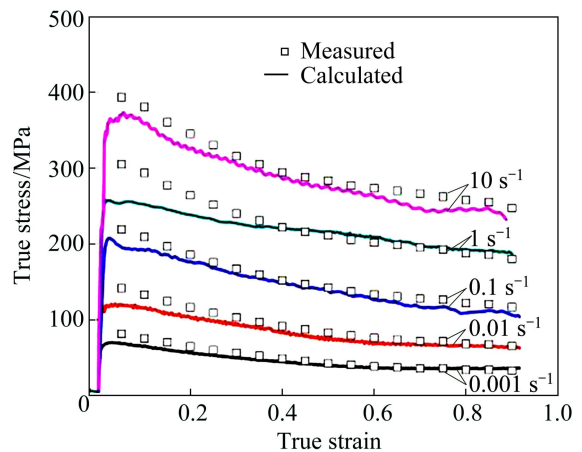


Fig. 6 Comparisons between predicted and measured flow

stress curves of electron beam weldments deformed at 940 °C
Table 1 Comparisons of calculated (σ_c) and measured (σ_m) flow stress values for cases with temperature of 940 °C

Strain	Strian rate/s ⁻¹	σ_c /MPa	σ_m /MPa	Error analysis	
				Error/%	Mean/%
0.1	0.001	64.57	75.32	13.12	10.76
	0.01	115.16	133.19	12.88	
	0.1	191.16	209.21	8.63	
	1	252.08	293.74	13.30	
	10	358.65	381.01	5.87	
0.3	0.001	49.51	56.06	11.68	6.75
	0.01	93.32	102.74	9.17	
	0.1	160.32	166.96	3.98	
	1	227.15	240.03	5.37	
	10	304.68	315.96	3.57	
0.5	0.001	39.50	42.53	7.12	5.12
	0.01	74.23	82.89	10.45	
	0.1	137.8	142.06	3.00	
	1	216.05	211.23	2.28	
	10	275.78	283.52	2.73	
0.7	0.001	35.63	35.51	0.34	4.81
	0.01	67.42	71.65	5.90	
	0.1	116.41	127.62	8.78	
	1	198.55	195.20	1.72	
	10	247.06	266.52	7.30	
0.9	0.001	34.96	32.85	6.42	5.08
	0.01	63.08	65.16	3.19	
	0.1	106.05	113.1	6.23	
	1	184.91	179.98	2.74	
	10	228.03	244.14	6.60	

3.3 Processing map for TC11/Ti–22Al–25Nb dual-alloy

In the past twenty years, processing map has been used to optimize the processing parameters in hot working of the metallic materials, such as titanium alloys [15–17], superalloys [27,28], and aluminium alloys [29,30]. According to the principles of DMM, the materials undergo the hot deformation can be considered as a power dissipater, which assumes that most of the instantaneous power P absorbed by work-piece is dissipated by the dissipative magnitude G , which is the power dissipated via the plastic deformation, and the dissipative coordination magnitude J , which is the work related to metallurgical evolution via different mechanisms such as phase transition, DRV and DRX. The ratio of $\partial J/\partial G$ is equivalent to the strain rate sensitivity exponent m . when m is 1, material is in an ideal linear dissipation state. The dissipative coordination magnitude J reaches the maximum $J_{\max} = \sigma\dot{\epsilon}/2$. By normalizing the instantaneous J with the maximum value,

the efficiency of power dissipation η can be defined as

$$\eta = \frac{J}{J_{\max}} = \frac{2m}{m+1} \quad (7)$$

The power dissipation map is obtained by plotting iso-efficiency contour map of the parameter η . A continuum criterion for the occurrence of flow instability is obtained by utilizing instability criterion established by PRASAD and SESHACHRYULU [31] which is shown as follows:

$$\xi(\dot{\epsilon}) = \frac{\partial \ln[m/(1+m)]}{\partial \ln \dot{\epsilon}} + m < 0 \quad (8)$$

where $\xi(\dot{\epsilon})$ is the instability parameter. The flow instability is predicted to occur when $\xi(\dot{\epsilon})$ becomes negative. The values of m can be calculated by differentiating the three-order polynomial fitting line of $\ln \dot{\epsilon} - \ln \sigma$ plots. Then, the efficiency of power dissipation (η) and the instability parameter (ξ) can be calculated by Eqs. (7) and (8), respectively. A processing map can be constructed by superimposing the instability map over the power dissipation map, from which the individual microstructure processes and the limiting conditions for the regimes of flow instability can be obtained.

Figure 7 shows the effects of strain on the efficiency of power dissipation (η) for TC11/Ti–22Al–25Nb dual-alloy under different strain rates and deformation temperatures. Obviously, the values of η are sensitive to the strain under the studied experimental condition and change gradually with the strain, deformation temperature and strain rate. When the strain rates are 0.01 (Fig. 7(b)), 0.1 (Fig. 7(c)) and 1 s⁻¹ (Fig. 7(d)), the η values increase with increasing the strain. Meanwhile, at the strain rate of 0.01 s⁻¹, the η maintains high values for all deformation temperatures. However, when the strain rates are larger or lower such as 10 s⁻¹ (Fig. 7(e)) and 0.001 s⁻¹ (Fig. 7(a)), the η values decrease with increasing the strain, except that there is a slight fluctuation under the deformation temperature of 900 °C. The efficiency of power dissipation can be used to indicate the dissipation of power induced by the microstructural evolution. Generally speaking, the domain with high efficiency of power dissipation has good workability for material. However, the higher efficiency of power dissipation does not mean better workability. It should be analyzed combined with the instability parameter (ξ).

The processing map of the EB weldments constructed at the strain of 0.90 is given in Fig. 8. In the map, the variation of efficiency of power dissipation (η) corresponds to the temperature and strain rate is represented as a contour map while the shaded region corresponds to the flow instability ($\xi(\dot{\epsilon}) < 0$).

The efficiency contours in the map have a curvature

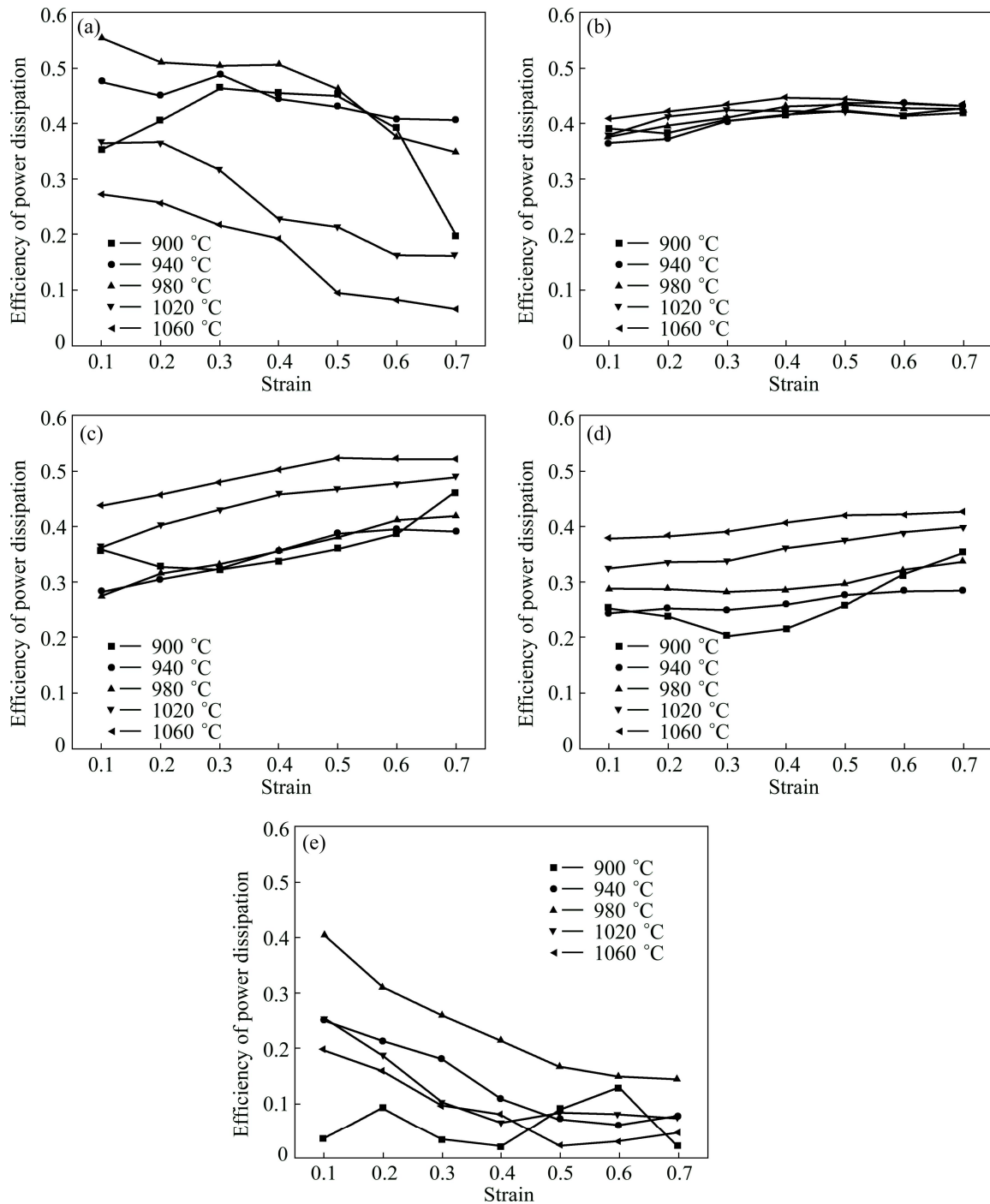


Fig. 7 Effects of strain on efficiency of power dissipation of dual-alloy with strain rates of 0.001 s⁻¹ (a), 0.01 s⁻¹ (b), 0.1 s⁻¹ (c), 1 s⁻¹ (d) and 10 s⁻¹ (e)

trajectory change in the temperature range of 960–970 °C, and a similar change is also observed at about 1000 °C. These changes are related to the phase transformation of the two alloys. For the TC11 alloy, the β transition temperature is about 1000 °C. Meanwhile, for the Ti-22Al-25Nb alloy, the phase transition temperature (at which $\beta/B2+O \rightarrow \alpha_2+\beta/B2+O$) is about 970 °C and other phase transition temperature (at which $\alpha_2+\beta/B2+O \rightarrow \alpha_2+\beta/B2$) is about 1010 °C. Such points

of change incurvature are also observed in the processing map of other alloy systems, which are associated with the occurrence of phase transformation and dissolution [11,18]. The peak efficiency of power dissipation about 0.51 in the map occurs at around 1060 °C and 0.1 s⁻¹. The domain appears to extend to moderate strain rate (0.01–0.1 s⁻¹), and may even reach high peak efficiency ($\eta > 0.40$).

The domains of processing map can be interpreted

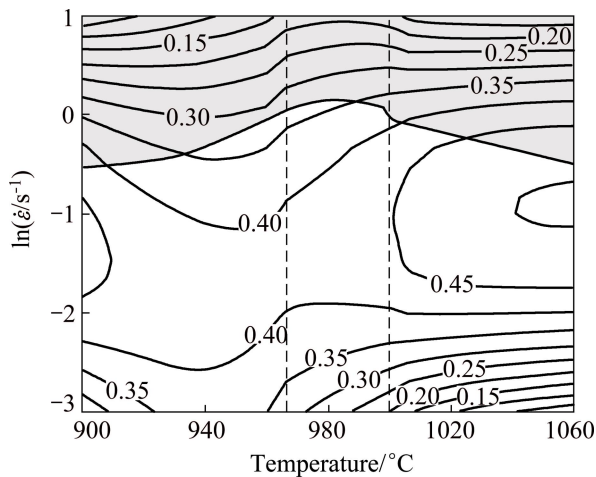


Fig. 8 Processing map of electron beam weldments processed with strain of 0.90 (Contour numbers indicate efficiency of power dissipation (η) and shaded region represents flow instability region)

based on the characteristic efficiency variation associated with the microstructural evolution [32,33]. The domains marked by the limiting conditions are designated as “safe” for processing. The deformation mechanisms of the safe domains include DRV, DRX and super-plasticity. Normally, the value of efficiency of power dissipation related to DRX is about 0.30–0.50, while that associated with super-plasticity is very high (about 0.60) [34,35]. The typical microstructures of the dual-alloy EB weldments processed after hot compression are shown in Figs. 9 and 10. The typical microstructures are all deformed at the strain rate of 0.1 s^{-1} and different temperatures. Under these conditions, the efficiency of power dissipation is high. Under the deformation condition of $900 \text{ }^\circ\text{C}$ and 0.1 s^{-1} , it can be seen that fine phases precipitate in grains along the direction of metal flow (Fig. 9(b)). In the heated affected zone (HAZ) of TC11 alloy, more lath-like α phases precipitate with strong direction performance as the deformation effect. Near the fusion zone, fine recrystallized β grains can be observed (Fig. 9(a)). It indicates that DRX occurs during the deformation process. As the deformation temperature increases, the microstructure of welding zone has changed. When the deformation temperature rises up to $1060 \text{ }^\circ\text{C}$ which exceeds the β phase transformation point of two alloys, the microstructure of welding zone mainly consists of β grains (Fig. 10). As mentioned above, the peak efficiency of power dissipation occurs at the region $1060 \text{ }^\circ\text{C}$ and 0.1 s^{-1} . The microstructure observation is conducted to validate the accuracy of DRX occurring under this condition. In the HAZ of TC11 alloy, the β grains are elongated along the deformation lines and the recrystallized grains can be found at the primary grain boundaries (Fig. 10(a)). In the fusion zone and HAZ of

Ti–22Al–25Nb, the DRX microstructures are more evident (Figs. 10(b) and (c)). It can be found that the primary grain boundaries become serrated and bulged. A few newly formed fine DRX grains are observed. Generally, DRX is a beneficial process during the hot deformation since it can provide stable flow and make the microstructure reconstituted.

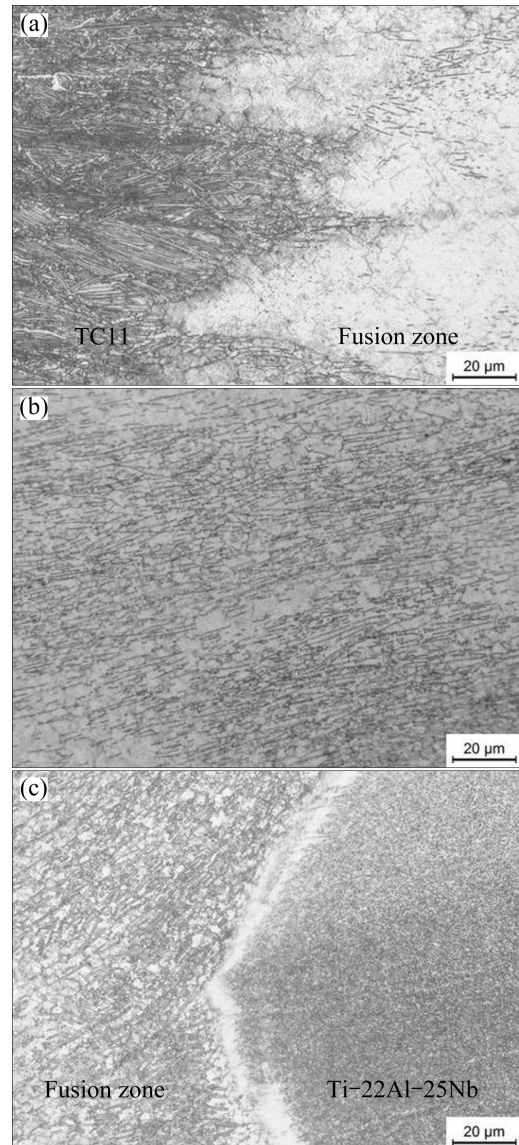


Fig. 9 Typical microstructures of TC11/Ti–22Al–25Nb dual-alloy deformed at strain of 0.90 under deformation condition of $900 \text{ }^\circ\text{C}$ and 0.1 s^{-1} ($\eta=0.46$): (a) Interface of TC11 alloy and fusion zone; (b) Fusion zone; (c) Interface of Ti–22Al–25Nb alloy and fusion zone

From the processing map (Fig. 8), it can be found that with decreasing the strain rate, the efficiency of power dissipation reduces sharply under the deformation temperature of $1060 \text{ }^\circ\text{C}$. Combined with the microstructures (Fig. 11), it can be found that the grains coarsen seriously. When the strain rate decreases, the specimens are kept at high temperature for longer time

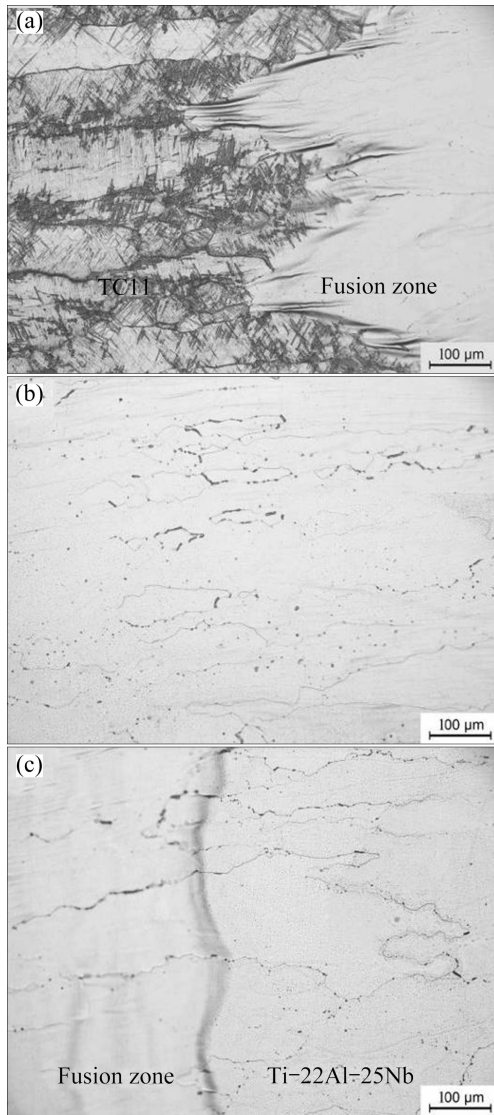


Fig. 10 Typical microstructures of TC11/Ti-22Al-25Nb dual-alloy deformed at strain of 0.90 under deformation condition of 1060 °C and 0.1 s^{-1} ($\eta=0.51$): (a) Interface of TC11 alloy and fusion zone; (b) Fusion zone; (c) Interface of Ti-22Al-25Nb alloy and fusion zone

and the work hardening rate is low, the deformation mechanism is dominated by DRV under this deformation condition. In addition, the processing map predicts a large instability domain located in the temperature range of 900–1060 °C with the strain rate higher than 0.6 s^{-1} . The microstructural evolution during the deformation is shown in Fig. 12. Figure 12(a) shows the metallograph at the temperature of 900 °C with the strain rate of 10 s^{-1} . It can be seen obviously that the adiabatic shear bands are present at an angle of 45° to the compressive axis, which is often observed in titanium alloys at low temperature and high strain rate. Figure 12(b) shows the metallograph at the temperature of 1060 °C with the strain rate of 10 s^{-1} , which presents the typical microstructure of flow localization in HAZ.

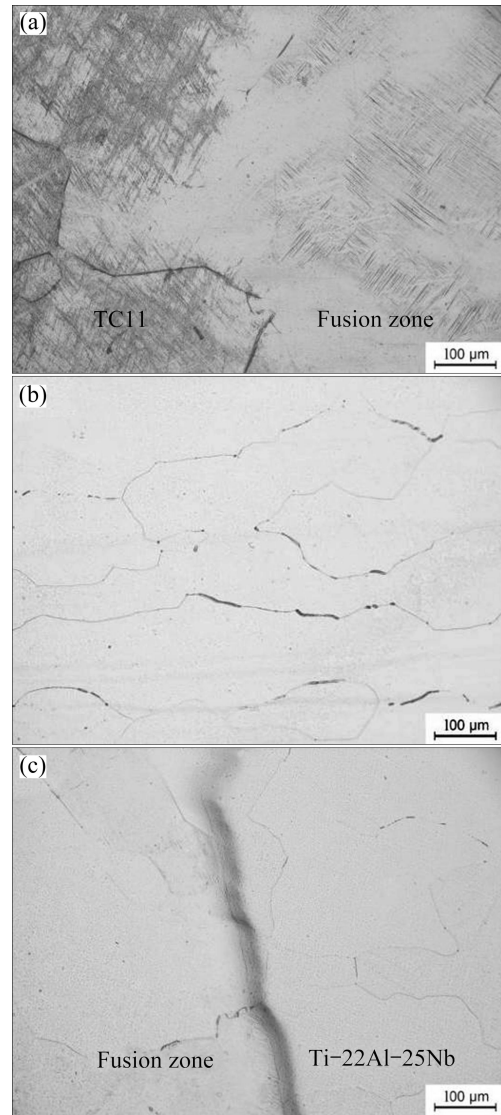


Fig. 11 Typical microstructures of TC11/Ti-22Al-25Nb dual-alloy deformed at strain of 0.90 under deformation condition of 1060 °C and 0.001 s^{-1} ($\eta=0.02$): (a) Interface of TC11 alloy and fusion zone; (b) Fusion zone; (c) Interface of Ti-22Al-25Nb alloy and fusion zone

4 Conclusions

1) The deformation temperature and strain rate affect the flow stress in the isothermal deformation of TC11/Ti-22Al-25Nb EB weldments significantly. The flow stress decreases with increasing the deformation temperature and decreasing the strain rate. The apparent activation energy of the EB weldments in the hot working process is calculated to be 334 kJ/mol, and a constitutive equation by which the flow stress is represented as a function of strain rate and deformation temperature, is designated as

$$\dot{\varepsilon} = 5.20 \times 10^{12} [\sinh(0.011\sigma)]^{3.05} \exp\left(\frac{-3.34 \times 10^5}{RT}\right)$$

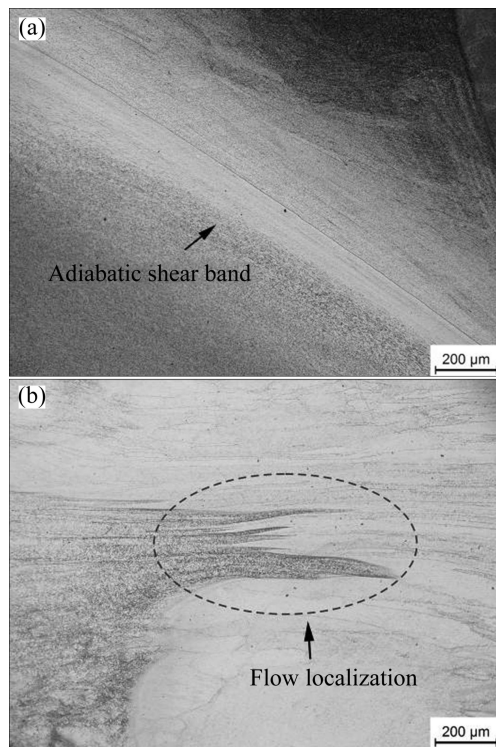


Fig. 12 Microstructures occurring in instability domain of electron beam weldments: (a) Adiabatic shear band under deformation condition of 900 °C and 10 s⁻¹; (b) Flow localization under deformation condition of 1060 °C and 10 s⁻¹

2) The apparent activation energy for deformation in isothermal compression of the EB weldments decreases with increasing the strain at all deformation temperatures. The relationship between the strain and the value of apparent activation energy is studied, and the 5th order polynomial function is built. The apparent activation energy value under different strains can be described well with the function.

3) The efficiency of power dissipation η obviously changes with the variation of deformation conditions. Under the strain rates of 0.01, 0.1 and 1 s⁻¹, the value of η increases with increasing the true strain at different deformation temperatures. While the value of η decreases under the strain rates of 0.001 and 10 s⁻¹ except that there is a slight fluctuation at the deformation temperature of 900 °C.

4) The hot working process can be carried out safely in the domain with the strain rate of 0.001–0.6 s⁻¹ and the temperatures of 900–1060 °C. When the height reduction is about 60%, the optimum processing condition is ($t_{opi}=1060$ °C, $\dot{\epsilon}_{opi}=0.1$ s⁻¹) with the peak efficiency of 0.51. Under this deformation, DRX is observed obviously in the microstructure of welding zone. Under the condition of 1060 °C and 0.001 s⁻¹, the deformation mechanism is dominated by DRV and the value of η decreases sharply ($\eta=0.02$).

References

- [1] TAN Li-jun, YAO Ze-kun, QIN Chun, GUO Hong-zhen, ZHANG Jian-wei. Effects of deformation temperature on microstructure and mechanical properties of electron beam welded joint of dissimilar titanium alloys [J]. The Chinese Journal of Nonferrous Metals, 2010, 20(8): 1533–1538. (in Chinese)
- [2] LIU Chuan, ZHANG Jian-xu, WU Bing, GONG Shui-li. Numerical investigation on the variation of welding stresses after material removal from a thick titanium alloy plate joined by electron beam welding [J]. Materials and Design, 2012; 34: 609–617.
- [3] ZHAO Xiao-hui, LIU Yu. Research on fatigue behavior of electron beam welding joint of 06Cr19Ni10 austenitic stainless steel sheet [J]. Materials and Design, 2014, 57: 494–502.
- [4] WANG Shao-gang, WU Xing-qiang. Investigation on the microstructure and mechanical properties of Ti–6Al–4V alloy joints with electron beam welding [J]. Materials and Design, 2012, 36: 663–670.
- [5] ZHANG Hong-tao, HE Peng, FENG Ji-cai, WU Hui-qiang. Interfacial microstructure and strength of the dissimilar joint Ti₃Al/TC4 welded by the electron beam process [J]. Materials Science and Engineering A, 2006, 425(1): 255–259.
- [6] SABOL J C, PASANG T, MISIOLEK W Z, WILLIAMS J C. Localized tensile strain distribution and metallurgy of electron beam welded Ti–5Al–5V–5Mo–3Cr titanium alloys [J]. Journal of Materials Processing Technology, 2012, 212(11): 2380–2385.
- [7] LIU Ying-ying, YAO Ze-kun, GUO Hong-zhen, YANG Hang-hang. Microstructure and property of the Ti–24Al–15Nb–1.5Mo/TC11 joint welded by electron beam welding [J]. International Journal of Minerals, Metallurgy and Materials, 2009, 16(5): 568–575.
- [8] TAN Li-jun, YAO Ze-kun, NING Yong-quan, GUO Hong-zhen. Effect of isothermal deformation on microstructure and properties of electron beam welded joint of Ti2AlNb/TC11 [J]. Materials Science and Technology, 2011, 27(9): 1469–1474.
- [9] LIN Y C, WEN D X, DENG J, LIU G, CHEN J. Constitutive models for high-temperature flow behaviors of a Ni-based superalloy [J]. Materials and Design, 2014, 59: 115–123.
- [10] SENTHILKUMAR V, BALAJI A, NARAYANASAMY R. Analysis of hot deformation behavior of Al5083–TiC nanocomposite using constitutive and dynamic material models [J]. Materials and Design, 2012, 37: 102–110.
- [11] NING Y, YAO Z, GUO H, FU M W. Hot deformation behavior and hot working characteristic of Nickel-base electron beam weldments [J]. Journal of Alloys and Compounds, 2014, 584: 494–502.
- [12] MCQUEEN H J, IMBERT C A C. Dynamic recrystallization: Plasticity enhancing structural development [J]. Journal of Alloys and Compounds, 2004, 378(1–2): 35–43.
- [13] MA Xiong, ZENG Wei-dong, TIAN Fei, ZHOU Yi-gang, SUN Yu. Optimization of hot process parameters of Ti–6.7Al–2Sn–2.2Zr–2.1Mo–1W–0.2Si alloy with lamellar starting microstructure based on the processing map [J]. Materials Science and Engineering A, 2012, 545: 132–138.
- [14] PRASAD Y V R K, SESHACHARYULU T, MEDEIROS S C, FRAZIER W G. Influence of oxygen content on the forging response of equiaxed ($\alpha+\beta$) preform of Ti–6Al–4V: Commercial vs. ELI grade [J]. Journal of Materials Processing Technology, 2001, 108(3): 320–327.
- [15] ZHANG X Y, LI M Q, LI H, LUO J, SU S B, WANG H. Deformation behavior in isothermal compression of the TC11 titanium alloy [J]. Materials and Design, 2010, 31(6): 2851–2857.
- [16] MA Xiong, ZENG Wei-dong, XU Bin, SUN YU, XUE Chen, HAN Yuan-fei. Characterization of the hot deformation behavior of a

- Ti-22Al-25Nb alloy using processing maps based on the Murty criterion [J]. *Intermetallics*, 2012, 20(1): 1–7.
- [17] SESHACHARYULU T, MEDEIROS S C, FRAZIER W G, PRASAD Y V R K. Hot working of commercial Ti-6Al-4V with an equiaxed α - β microstructure: Materials modeling considerations [J]. *Materials Science and Engineering A*, 2000, 284(1–2): 184–194.
- [18] LI A B, HUANG L J, MENG Q Y, GENG L, CUI X P. Hot working of Ti-6Al-3Mo-2Zr-0.3Si alloy with lamellar α + β starting structure using processing map [J]. *Materials and Design*, 2009, 30(5): 1625–1631.
- [19] JIA Jian-bo, ZHANG Kai-feng, LIU Li-ming, WU Fu-yao. Hot deformation behavior and processing map of a powder metallurgy Ti-22Al-25Nb alloy [J]. *Journal of Alloys and Compounds*, 2014, 600: 215–221.
- [20] WANG Tao, LI Zhao, FU Shu-hong, ZHANG Yong, ZHAO Yu-xin, GUO Ling. Hot deformation behavior and microstructure of U720Li alloy [J]. *Advanced Materials Research*, 2013, 709: 143–7.
- [21] PILEHVA F, ZAREI-HANZAKI A, GHANBARI M, ABEDI H R. Flow behavior modeling of a Ti-6Al-7Nb biomedical alloy during manufacturing at elevated temperatures [J]. *Materials and Design*, 2013, 51: 457–465.
- [22] NANDY T K, BANERJEE D. Deformation mechanisms in the O phase [J]. *Intermetallics*, 2000, 8(9–11): 1269–1282.
- [23] NANDY T K, BANERJEE D. Creep of the orthorhombic phase based on the intermetallic Ti₂AlNb [J]. *Intermetallics*, 2000, 8(9–11): 915–928.
- [24] CHEN Hui-qing, CAO Chun-xiao. Characterization of hot deformation microstructures of alpha-beta titanium alloy with equiaxed structure [J]. *Transactions of Nonferrous Metals Society of China*, 2012, 22(3): 503–509.
- [25] CHEN Hui-qing, CAO Chun-xiao, GUO Ling, LIN Hai. Hot deformation mechanism and microstructure evolution of TC11 titanium alloy in β field [J]. *Transactions of Nonferrous Metals Society of China*, 2008, 18(5): 1021–1027.
- [26] WU K, LIU G Q, HU B F, WANG C Y, ZHANG Y W, TAO Y, LIU J T. Effect of processing parameters on hot compressive deformation behavior of a new Ni-Cr-Co based P/M superalloy [J]. *Materials Science and Engineering A*, 2011, 528(13–14): 4620–4629.
- [27] ZHOU Ge, DING Hua, CAO Fu-rong, HAN Yin-ben, ZHANG Bei-jiang. Flow instability criteria in processing map of superalloy GH79 [J]. *Transactions of Nonferrous Metals Society of China*, 2012, 22(7): 1575–1581.
- [28] NING Y, FU M W, CHEN X. Hot deformation behavior of GH4169 superalloy associated with stick δ phase dissolution during isothermal compression process [J]. *Materials Science and Engineering A*, 2012, 540: 164–173.
- [29] CHEN Song-yi, CHEN Kang-hua, PENG Guo-sheng, JIA Le. Effect of initial microstructure on hot workability of 7085 aluminum alloy [J]. *Transactions of Nonferrous Metals Society of China*, 2013, 23(4): 956–963.
- [30] LIN Y C, LI L T, XIA Y C, JIANG Y Q. Hot deformation and processing map of a typical Al-Zn-Mg-Cu alloy [J]. *Journal of Alloys and Compounds*, 2013, 550: 438–445.
- [31] PRASAD Y V R K, SESHACHRYULU T. Modeling of hot deformation for microstructural control [J]. *International Materials Reviews*, 1988, 43(6): 243–258.
- [32] RAO K P, PRASAD Y V R K, SURESH K. Hot working behavior and processing map of a γ -TiAl alloy synthesized by powder metallurgy [J]. *Materials and Design*, 2011, 32(10): 4874–4881.
- [33] ZHANG Tian, TAO You-rui, WANG Xue-yin. Constitutive behavior, microstructural evolution and processing map of extruded Al-1.1Mn-0.3Mg-0.25RE alloy during hot compression [J]. *Transactions of Nonferrous Metals Society of China*, 2014, 24(5): 1337–1345.
- [34] MEDEIRO S C, PRASAD Y V R K, FRAZIER W G, SRINIVASAN R. Microstructural modeling of metadynamic recrystallization in hot working of IN 718 superalloy [J]. *Materials Science and Engineering A*, 2000, 293(1–2): 198–207.
- [35] PRASAD Y V R K, SESHACHRYULU T, MEDEIRO S C, FRAZIER W G. Effect of preform microstructure on the hot working mechanisms in ELI grade Ti-6Al-4V: Transformed β v. equiaxed (α + β) [J]. *Materials Science and Technology*, 2000, 16(5): 511–520.

TC11/Ti-22Al-25Nb 双合金的热变形行为

秦春, 姚泽坤, 宁永权, 石志峰, 郭鸿镇

西北工业大学 材料学院, 西安 710072

摘要: 在温度为 900~1060 °C 和应变速率为 0.001~10 s⁻¹ 的条件下, 通过热模拟压缩实验研究 TC11/Ti-22Al-25Nb 双合金电子束焊接件的高温热变形行为。结合实验数据, 建立双合金热变形中流变应力随应变速率和变形温度的本构方程。同时对变形过程中的激活能进行计算和分析得出, 激活能随着应变的增加而逐渐减小。在应变为 0.9 时激活能为 334 kJ/mol。变形过程中耗散率 η 随着变形参数的变化而变化; 当应变速率为 0.01、0.1 和 1 s⁻¹ 时, η 随应变的增加而增加; 而当应变速率为 0.001 和 10 s⁻¹ 时, η 随应变的增加而减小。通过热加工图分析可知, 最大耗散率($\eta=0.51$) 出现在 1060 °C 和 0.1 s⁻¹, 在此条件下, 可以从焊缝区域组织中观察到明显的动态再结晶现象。而当应变速率降低时, 耗散率 η 急剧下降, 在 1060 °C 和 0.001 s⁻¹ 的变形条件下, η 降低到 0.02, 变形机制以动态回复为主。当失稳系数 $\zeta(\dot{\epsilon})$ 为负时, 材料高温变形发生失稳。分析可知, 应变速率为 0.001~0.6 s⁻¹, 变形温度为 900~1060 °C 是双合金热变形的安全区域。

关键词: 双合金; 热变形; 加工图; 激活能; 显微组织